

Low-momentum anticorrelated electron emission in mid-infrared double ionization of argon

Shiwei Liu(刘士炜), Zongqiang Yuan(袁宗强), and Difa Ye(叶地发)

Citation: Chin. Phys. B, 2026, 35 (**8**): 083206. DOI: 10.1088/1674-1056/ae85fb
http://cpb.iphy.ac.cn; http://iopscience.iop.org/cpb

What follows is a list of articles you may be interested in

Relative phase-dependent two-electron emission dynamics with two-color circularly polarized laser fields

Tong-Tong Xu(徐彤彤), Lian-Lian Zhang(张莲莲), Zhao Jin(金钊), Wei-Jiang Gong(公卫江)
Chin. Phys. B, 2020, 29 (**9**): 093202. DOI: 10.1088/1674-1056/ab928c

Controlling electron collision by counterrotating circular two-color laser fields

Baoqin Li(李宝琴), Xianghe Ren(任向河), Jingtao Zhang(张敬涛)
Chin. Phys. B, 2020, 29 (**4**): 043202. DOI: 10.1088/1674-1056/ab7907

Relative phase effect of nonsequential double ionization in Ar by two-color elliptically polarized laser field

Jia-He Chen(陈佳贺), Tong-Tong Xu(徐彤彤), Tao Han(韩涛), Yue Sun(孙悦), Qing-Yun Xu(徐清芸), Xue-Shen Liu(刘学深)
Chin. Phys. B, 2020, 29 (**1**): 013203. DOI: 10.1088/1674-1056/ab5d03

Effect of elliptical polarizations on nonsequential double ionization in two-color elliptically polarized laser fields

Tong-Tong Xu(徐彤彤), Jia-He Chen(陈佳贺), Xue-Fei Pan(潘雪飞), Hong-Dan Zhang(张宏丹), Shuai Ben(贲帅), Xue-Shen Liu(刘学深)
Chin. Phys. B, 2018, 27 (**9**): 093201. DOI: 10.1088/1674-1056/27/9/093201

Effect of electron excitation in nonsequential double ionization by intense laser fields

Xiang Chen(陈翔), Qiujing Han(韩秋静), Jingtao Zhang(张敬涛)
Chin. Phys. B, 2018, 27 (**7**): 073202. DOI: 10.1088/1674-1056/27/7/073202

Low-momentum anticorrelated electron emission in mid-infrared double ionization of argon

Shiwei Liu(刘士炜)[1], Zongqiang Yuan(袁宗强)[2], and Difa Ye(叶地发)[3,†]

[1] *School of Science, Beijing University of Civil Engineering and Architecture, Beijing* 100044, *China*
[2] *Science and Technology on Plasma Physics Laboratory, Research Center of Laser Fusion, China Academy of Engineering Physics, Mianyang* 621900, *China*
[3] *National Key Laboratory of Computational Physics, Institute of Applied Physics and Computational Mathematics, Beijing* 100088, *China*

(Received 7 May 2026; revised manuscript received 29 June 2026; accepted manuscript online 3 July 2026)

We investigate wavelength-dependent nonsequential double ionization of Ar from the near- to mid-infrared regime using a full-Coulomb three-dimensional semiclassical ensemble model. As the wavelength increases from 800 nm and 1300 nm to 3100 nm, the correlated two-electron momentum distribution evolves from a fingerlike pattern to a crosslike pattern and develops low-momentum anticorrelated electron emission in quadrants II and IV. Trajectory analysis shows that the fingerlike structures are associated with Coulomb-assisted large-angle backscattering, whereas the mid-infrared spectrum gives larger weight to forward-scattering-like recollision trajectories and small longitudinal momenta. The low-momentum anticorrelated component does not arise from prompt impact ionization at recollision. Instead, recollision prepares a correlated or excited near-core configuration that completes double escape in a later field window near an electric-field maximum, where the vector-potential contribution to the longitudinal drift is small. These results show that high-U_p anticorrelated electron emission is shaped jointly by recollision energy transfer and by the field phase at final escape.

Keywords: nonsequential double ionization, recollision dynamics, mid-infrared strong laser fields, semiclassical trajectory model

PACS: 32.80.Rm, 32.80.Fb, 34.80.Dp, 31.15.xg

DOI: 10.1088/1674-1056/ae85fb **CSTR:** 32038.14.CPB.ae85fb

1. Introduction

Laser-driven rescattering provides a subcycle route by which a strong laser field converts tunneling ionization into a probe of electron correlation. In the three-step picture, an electron released near a field maximum is driven back to the parent ion with a kinetic energy up to approximately $3.17U_p$,[1] where $U_p = E_0^2/(4\omega^2)$ is the ponderomotive energy with electric field amplitude E_0 and laser frequency ω. Nonsequential double ionization (NSDI) is the paradigmatic two-electron manifestation of this mechanism: the returning electron releases or excites a second electron, producing correlated double emission beyond independent sequential ionization.[2,3] Kinematically complete measurements transformed this yield enhancement into a differential observable, showing that longitudinal and transverse two-electron momenta encode energy sharing at recollision, binary and recoil scattering, and post-collision Coulomb correlation.[4–8] NSDI has thus become a prototypical process for reading few-body electron correlation from laser-driven momentum spectra.[9]

The recollision step can lead to double emission through two limiting time orderings. In recollision-impact ionization, or the direct $(e,2e)$ channel, the returning electron transfers sufficient energy to the bound electron during an inelastic electron-impact collision, so that double escape is initiated promptly at recollision. In recollision-induced excitation with subsequent ionization (RESI), the recollision deposits energy into an excited ionic configuration without immediately removing the second electron; the excited electron is subsequently ionized by the laser field.[10–14] The distinction between impact ionization and excitation tunneling was established in Ar by recoil-ion and electron momentum imaging.[10] In He, fully differential measurements resolved binary and recoil collision branches and mapped the correlated two-electron momentum distribution.[7,8,15] Semiclassical trajectory analysis further traced the finger-like structures to Coulomb-assisted large-angle backscattering near the ionic core.[16] Near or below the recollision threshold, multiple recollisions, intermediate excited states, and quantum interference can substantially modify the correlated two-electron momentum distributions produced by recollision-induced excitation and subsequent field ionization.[17–23] Consequently, prompt double emission primarily reflects the recollision phase, energy sharing, and near-core scattering, whereas delayed double emission is sensitive to the excitation step and to the field phase at which ionization is completed.

The mid-infrared regime provides a test of this recollision-based picture. Since $U_p \propto I\lambda^2$, longer wavelengths increase the maximum return energy, and one might first ex-

†Corresponding author. E-mail: ye_difa@iapcm.ac.cn

© 2026 Chinese Physical Society and IOP Publishing Ltd. All rights, including for text and data mining, AI training, and similar technologies, are reserved.

pect the near-infrared NSDI spectrum to expand mainly with the scale $\sqrt{U_p}$. Such a ponderomotive scaling, however, does not by itself determine the correlated momentum distribution. Energy-domain observables in strong-field double ionization can obey useful scaling laws,[24] but the correlated two-electron momentum distribution retains additional information on return time, near-core scattering, and post-recollision propagation. Mid-infrared fields lengthen the electron excursion and increase wave-packet spreading before return. As a result, the measured spectrum becomes sensitive not only to the increased return energy, but also to the modified return flux, Coulomb focusing, and multiple returns.[25,26] Wavelength-dependent NSDI measurements in Xe have shown clear deviations from simple-man scaling and an intensity-dependent redistribution between recollision-impact ionization and RESI-like contributions.[27–30] Recent higher-order S-matrix and frequency-dependent quantum calculations further demonstrate that Coulomb interactions and laser frequency can reshape final electron and ion momentum spectra beyond a simple ponderomotive rescaling.[31,32] Thus, mid-infrared NSDI is not merely the high-return-energy limit of the near-infrared problem. Long-wavelength propagation changes the relative weights of first and later returns, near-core scattering, and post-recollision field-ionization pathways, and these changes are directly reflected in the final correlated momentum spectrum.[33]

Recently, a mid-infrared rare-gas NSDI study[34] in Ar suggests that, at 3100 nm, where U_p exceeds 80 eV, the measured longitudinal two-electron momentum distribution exhibits a localized low-momentum anticorrelation in quadrants II and IV. In the usual recollision picture, the electron returns close to a zero of the electric field, where the vector potential is large; prompt release at that instant therefore produces sizable longitudinal drift momenta. The appearance of anticorrelated electron pairs with small final momenta indicates that part of the correlated two-electron ensemble survives the recollision and escapes in a later field window. The relevant dynamical variable is then not only the recollision energy, but the phase at which the correlated system finally decouples from the ionic core. This emphasis on emission timing and field phase is in line with recent attoclock measurements of correlated-electron emission and with theoretical studies showing that recollision-induced-excitation pathways leave final two-electron momentum distributions that depend on event dominance, field symmetry, and quantum interference.[35–38]

In this work, we employ a semiclassical simulation to analyze the wavelength-dependent evolution of the correlated photo-electron momentum distributions (PMD) and to characterize the trajectory ensemble associated with the localized low-P_r anticorrelation. The model launches the first electron by Ammosov–Delone–Krainov (ADK) tunneling, samples the initially bound electron from a microcanonical distribution, propagates both electrons with electron–ion and electron–electron Coulomb interactions, and includes field-driven tunneling from transient excited states. The calculated spectra show that the high-momentum finger-like structures at 800 nm and 1300 nm are associated with the backscattering branch of the recollision dynamics, where a close near-core encounter and Coulomb-assisted large-angle deflection generate large longitudinal drift momenta. At 3100 nm, the PMD is no longer dominated by the outer backscattering branch, but is characterized by forward-scattering-like recollision processes, which are manifested as a crosslike central structure. In contrast, the localized low-P_r component is traced to recollision-induced excitation followed by delayed field ionization near an electric-field maximum.

The paper is organized as follows. Section 2 introduces the semiclassical model. Section 3 presents the calculated wavelength-dependent momentum distributions and the analysis. Section 4 summarizes the main conclusions.

2. Semiclassical model

We employ a three-dimensional two-active-electron semiclassical model[39] for argon, and atomic units are used throughout unless otherwise stated. The laser field is linearly polarized along the z axis,

$$\boldsymbol{E}(t) = E_0 f(t)\cos(\omega t)\hat{\boldsymbol{z}}, \tag{1}$$

with a ten-cycle flat-top envelope followed by a three-cycle $\cos^2$ turnoff. The ionization potentials are chosen as $I_{p1} = 0.5791$, $I_{p2} = 1.0154$, corresponding to the first and second ionization potentials of Ar.

The first electron is released by tunnel ionization. Its ionization time t_0 is sampled within the flat-top part of the pulse according to an ADK-type quasistatic tunneling weight,[40] including the transverse-momentum factor,

$$W(t_0, p_\perp) \propto \exp\left(-\frac{2\kappa^3}{3|E(t_0)|}\right)\exp\left(-\frac{\kappa p_\perp^2}{|E(t_0)|}\right), \tag{2}$$

where $\kappa = \sqrt{2I_{p1}}$. The longitudinal velocity at the tunnel exit is set to zero. The exit position is obtained from the outer root of the field-lowered Coulomb barrier along the polarization direction. The second electron is initialized from a microcanonical distribution with binding energy $-I_{p2}$ in the Coulomb field of the residual ionic core.[39,41,42]

After initialization, both electrons are propagated in the laser field with the electron–core attraction and electron–electron repulsion retained throughout the pulse. Their equations of motion are

$$\frac{\mathrm{d}^2\boldsymbol{r}_i}{\mathrm{d}t^2} = -\boldsymbol{E}(t) - \nabla_i\left(V_{\mathrm{core}}(r_i) + V_{\mathrm{ee}}\right), \quad i = 1,2, \tag{3}$$

where

$$V_{\rm core}(r_i) = -\frac{2}{|\boldsymbol{r}_i|}, \quad V_{\rm ee} = \frac{1}{|\boldsymbol{r}_1 - \boldsymbol{r}_2|}. \tag{4}$$

Here $V_{\rm core}$ represents the effective Coulomb field of the residual Ar^{2+} core acting on the two active electrons. Equations (3) and (4) are integrated with an adaptive fourth–fifth-order Runge–Kutta algorithm.

To include field ionization from transient excited configurations generated after recollision, we follow the recollision-induced excitation-tunneling treatment of Ref. [12]. For an electron that remains bound, a WKB tunneling probability is evaluated when the electron reaches a classical outer turning point on the barrier-lowering side of the instantaneous laser field. Operationally, this corresponds to a turning point of the longitudinal motion, $p_{i,z} = 0$, with $z_i E(t) < 0$. The one-dimensional tunneling probability along the polarization direction is

$$P_i^{\rm WKB} = \exp\left(-2\sqrt{2}\int_{z_i^{\rm in}}^{z_i^{\rm out}} \sqrt{V_i(z,t) - V_i(z_i^{\rm in},t)}\,{\rm d}z\right), \tag{5}$$

where

$$V_i(z_i,t) = V_{\rm core}\left(\sqrt{x_i^2 + y_i^2 + z_i^2}\right) + E(t) z_i. \tag{6}$$

Here x_i and y_i are kept fixed during the one-dimensional barrier calculation, $z_i^{\rm in}$ is the instantaneous inner turning point, and $z_i^{\rm out}$ is the outer root of the field-distorted barrier satisfying $V_i(z_i^{\rm out},t) = V_i(z_i^{\rm in},t)$ with $|z_i^{\rm out}| > |z_i^{\rm in}|$. The occurrence of tunneling is sampled with the probability $P_i^{\rm WKB}$. After tunneling, the electron is launched from $z_i^{\rm out}$ and is propagated classically under the laser field and the full Coulomb interactions.

For each electron we monitor the single-electron field-free energy with respect to the ionic core,

$$\varepsilon_i(t) = \frac{p_i^2(t)}{2} + V_{\rm core}\left(r_i(t)\right). \tag{7}$$

The individual ionization time t_i is defined as the last time at which $\varepsilon_i(t)$ changes from negative to positive during the pulse. The double-ionization time used in the phase analysis is $t_{\rm ion} = \max(t_1, t_2)$. A trajectory is counted as double ionized when both electrons have positive field-free energies after the laser pulse and continue to escape during the subsequent propagation. In the numerical implementation, momenta are recorded after a long field-free interval so that the low-momentum part of the spectrum is converged.

The recollision time $t_{\rm r}$ is taken as the time of minimum electron–electron separation during the correlated return of the tunneled electron. The delay between recollision and final double emission is therefore $\Delta t = t_{\rm ion} - t_{\rm r}$. For the low-$P_{\rm r}$ trajectories analyzed below, the delayed release is preceded by a near-core recollision at $t_{\rm r}$, identified by the minimum electron–electron separation, during which the bound electron gains energy but does not escape promptly. The later field ionization is therefore assigned to a recollision-induced-excitation pathway with delayed ionization, rather than sequential double ionization. The final observables are the asymptotic longitudinal momenta $p_{1,z}$ and $p_{2,z}$ along the laser polarization direction. Because the two detected electrons are indistinguishable in the experiment, the calculated momentum distributions are symmetrized with respect to electron exchange when compared with the measured two-electron spectra.

To interpret the momentum structures associated with prompt impact ionization, we use the standard simple-man kinematics of the recollision model as a reference. The vector potential is defined by $\boldsymbol{E}(t) = -{\rm d}\boldsymbol{A}(t)/{\rm d}t$. For a monochromatic field,

$$E(t) = E_0\cos(\omega t), \quad A(t) = -\frac{E_0}{\omega}\sin(\omega t), \tag{8}$$

an electron released at t_0 with zero initial longitudinal velocity has, in the absence of Coulomb forces,

$$z(t) = \frac{E_0}{\omega}\sin(\omega t_0)(t - t_0) + \frac{E_0}{\omega^2}\left(\cos(\omega t) - \cos(\omega t_0)\right), \tag{9}$$

$$v_z(t) = \frac{E_0}{\omega}\left(\sin(\omega t_0) - \sin(\omega t)\right). \tag{10}$$

The return time $t_{\rm r}$ follows from $z(t_{\rm r}) = 0$, and the return energy is

$$E_{\rm r} = \frac{v_z^2(t_{\rm r})}{2} = 2U_{\rm p}\left(\sin(\omega t_0) - \sin(\omega t_{\rm r})\right)^2. \tag{11}$$

Within the Volkov approximation,[9,43,44] a final drift momentum $p_{i,z}$ corresponds to an instantaneous longitudinal velocity $p_{i,z} + A(t)$ at time t. Thus, for prompt impact ionization at the recollision time $t_{\rm r}$, the longitudinal kinetic-energy balance may be written as

$$\frac{[p_{1,z} + A(t_{\rm r})]^2}{2} + \frac{[p_{2,z} + A(t_{\rm r})]^2}{2} \simeq E_{\rm r} - I_{\rm p2}, \tag{12}$$

where $E_{\rm r}$ is the returning-electron energy. If the struck electron leaves the collision region with small longitudinal velocity, Eq. (12) gives

$$p_{2,z} \simeq -A(t_{\rm r}), \quad p_{1,z} \simeq -A(t_{\rm r}) \pm \sqrt{2(E_{\rm r} - I_{\rm p2})}. \tag{13}$$

The two signs correspond to the two limiting longitudinal scattering geometries of the returning electron: reversal of the longitudinal velocity after the collision gives a backscattering-like trajectory, while preservation of the incident direction gives a forward-scattering-like trajectory. The backscattering-like branch represents trajectories in which the returning electron experiences a close encounter with the ionic core after the recollision and undergoes Coulomb-assisted large-angle deflection, resulting in a reversal of its longitudinal velocity. The subsequent laser-driven acceleration converts this reversed velocity into large asymptotic drift momenta, forming the outer

fingerlike extensions of the PMD. By contrast, the forward-scattering-like branch represents trajectories in which the recolliding electron emerges from the collision region with its longitudinal direction largely preserved.

To isolate the anticorrelated component, we follow the sector analysis used in the near- and mid-infrared experiment.[34] In the final longitudinal momentum plane we define the polar angle ϕ measured counterclockwise from the positive $p_{1,z}$ axis. Events in quadrants II and IV are selected within the angular sectors

$$105^\circ < \phi < 165^\circ, \quad 285^\circ < \phi < 345^\circ. \tag{14}$$

The normalized radial momentum in these sectors is

$$P_\mathrm{r} = \frac{\sqrt{(p_{1,z})^2 + (p_{2,z})^2}}{\sqrt{U_\mathrm{p}}}. \tag{15}$$

When radial spectra are plotted, the event counts are weighted by $1/P_\mathrm{r}$ to remove the two-dimensional radial Jacobian, following the experimental sector analysis.[34] We further divide the selected events into a low-momentum region A, $P_\mathrm{r} \leq 1$, and a higher-momentum region B, $P_\mathrm{r} > 1$. This A/B separation is not a microscopic channel assignment. It is a diagnostic filter used to test whether low- and high-momentum anticorrelated events differ in their final field phase and in the delay between recollision and escape. The central quantity examined below is the vector potential at the final double-ionization time, $A(t_\mathrm{ion})$; low-P_r anticorrelation is expected when the final escape occurs near an electric-field maximum, where $A(t_\mathrm{ion}) \simeq 0$.

3. Results and discussion

3.1. Wavelength-dependent transition of the correlated momentum spectrum

Figure 1 shows the calculated longitudinal PMD of Ar for the wavelength-intensity matrix summarized in Table 1. The corresponding ponderomotive energy spans from the near-infrared to the high-U_p mid-infrared regime, with $3.17U_\mathrm{p}$ reaching up to several hundred eV at 3100 nm.

Table 1. Laser parameters used for the wavelength–intensity scan in Fig. 1.

Wavelength λ (nm)	Intensity (10^{14} W·cm^{-2})	U_p (a.u.)
800	0.9	0.198
800	1.5	0.329
800	2.0	0.439
800	2.8	0.615
1300	0.9	0.522
1300	1.5	0.870
1300	2.0	1.160
1300	2.8	1.624
3100	0.9	2.968
3100	1.5	4.946
3100	2.0	6.595
3100	2.8	9.233

The simple-man curves in Fig. 1 provide a kinematic comparison with prompt recollision-impact ionization. A final momentum $p_{i,z}$ corresponds to an instantaneous longitudinal velocity $p_{i,z} + A(t_\mathrm{r})$ at the recollision time. The longitudinal energy balance then gives Eq. (12). The two limiting signs correspond to backscattering-like and forward-scattering-like recollision geometries, shown by the white and purple curves, respectively. The wavelength evolution in Fig. 1 connects two familiar momentum-space structures in strong-field double ionization: near-infrared fingerlike spectra associated with Coulomb-assisted large-angle backscattering, and crosslike spectra previously observed in few-cycle or near-single-cycle fields.[7,8,45–48] Here the crosslike pattern occurs instead in a high-U_p mid-infrared regime. The comparison with the simple-man branches indicates that the global reshaping is associated primarily with the changing relative weight of near-core backscattering and forward-scattering-like recollision trajectories. The localized low-P_r anticorrelated component involves an additional timing effect and is analyzed separately below.

At the lowest intensity in 800 nm, the maximum return energy is below or close to the threshold for direct recollision-impact ionization, so that the simple-man loci do not account for the full distribution. The finite structures in quadrants II and IV indicate a significant RESI contribution in this near-threshold regime, where recollision-induced excitation is followed by subsequent field ionization. With increasing intensity, the available return energy increases, the RESI-related structures are reduced, and the correlated lobes in quadrants I and III develop into clearer fingerlike extensions. These high-momentum extensions indicate the increasing role of Coulomb-assisted large-angle backscattering in the direct recollision channel. At 1300 nm, the fingerlike structures remain the dominant high-momentum feature of the PMDs, but extend over a larger region along the diagonal directions in the normalized momentum plane. The spectra continue to follow the backscattering-like branch over a broad range of intensities, indicating that Coulomb-assisted backscattering still organizes the main high-momentum part of the distribution while the larger U_p modifies the accessible recollision energy. At 3100 nm, the recollision occurs in a different kinematic regime. Because of the higher U_p, the returning electron approaches the ionic core with higher longitudinal velocity after a longer excursion, so that only a smaller fraction of trajectories undergoes the close Coulomb deflection required for backscattering. The recolliding electron therefore tends to leave the collision region with its incident longitudinal direction retained, shifting the PMD away from the outer backscattering extensions and toward the forward-scattering-like branch, which gives the spectrum its crosslike central structure.

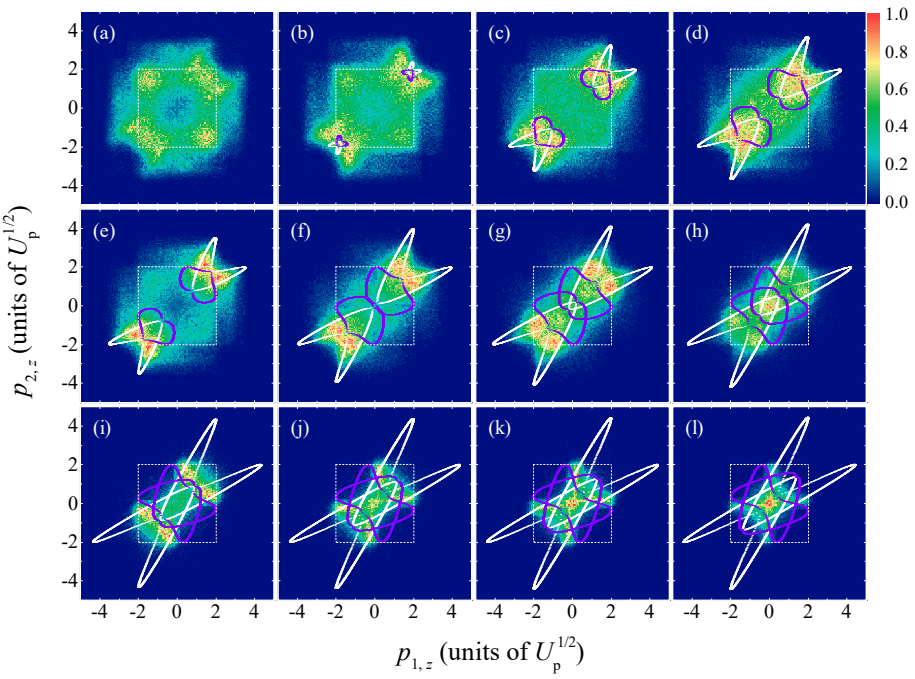


Fig. 1. Longitudinal two-electron momentum distributions of Ar from the full-Coulomb semiclassical calculation. Rows correspond to 800 nm, 1300 nm, and 3100 nm; columns correspond to peak intensities 0.9×10^{14} W/cm^2, 1.5×10^{14} W/cm^2, 2.0×10^{14} W/cm^2, and 2.8×10^{14} W/cm^2. Momenta are normalized by $\sqrt{U_p}$. White and purple curves denote the simple-man kinematic loci for backscattering-like and forward-scattering-like recollision trajectories, respectively.

3.2. Low-momentum anticorrelation

We select events in the angular sectors defined in Eq. (14) and analyze the normalized radial momentum P_r defined in Eq. (15). This sector selection is used as a diagnostic of anticorrelated emission, not as a one-to-one assignment of trajectories to a specific microscopic ionization pathway. It separates electron pairs with opposite longitudinal momenta according to the magnitude of their final drift momentum. Region A, $P_r \leq 1$, contains the localized low-momentum component, whereas region B, $P_r > 1$, contains the higher-momentum anticorrelated tail. Figure 2 compares the calculated P_r distributions with the experimental distributions of Ref. [34]. At 800 nm, the anticorrelated signal extends over a broad radial range; at 1300 nm, the distribution remains broad but shifts toward smaller P_r. At 3100 nm, by contrast, the anticorrelated sector is strongly concentrated at low P_r. With increasing wavelength, wave-packet spreading during the extended excursion before recollision reduces the near-core return flux and thus weakens prompt recollision-impact ionization, which requires a close recollision and efficient energy transfer. As a result, the high-P_r contribution in the anticorrelated sector becomes less prominent. The low-P_r sector is then more strongly associated with recollision-induced excitation followed by delayed field ionization. At 3100 nm, this delayed field-ionization step occurs preferentially near electric-field maxima, and therefore produces small final drift momenta.

Anticorrelation and low momentum carry different information. The signs of $p_{1,z}$ and $p_{2,z}$ specify the final longitudinal hemispheres of the two electrons, whereas P_r measures the drift-momentum scale. If both electrons were released

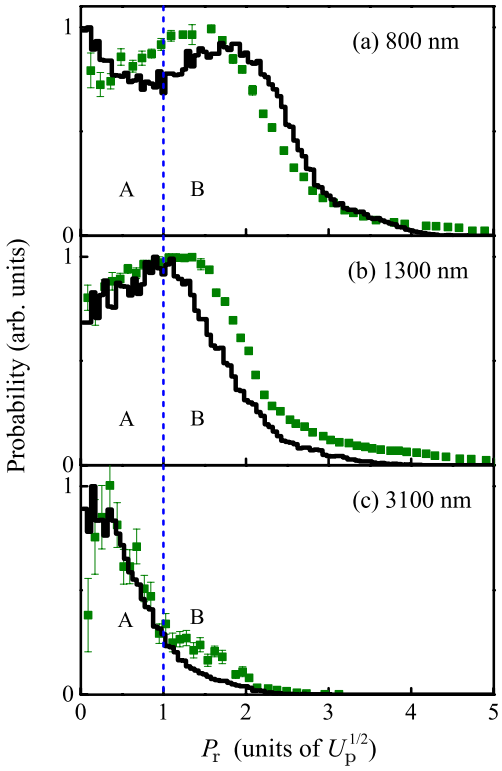


Fig. 2. Radial momentum distributions in the anticorrelated sectors for (a) 800 nm, 1.5×10^{14} W$\cdot$cm^{-2}, (b) 1300 nm, 1.5×10^{14} W/cm^{-2}, and (c) 3100 nm, 0.9×10^{14} W$\cdot$cm^{-2}. The radial coordinate is Eq. (15), with events selected by the angular sectors of Eq. (14). Symbols are the experimental data of Ref. [34]; solid curves are the present semiclassical results. The dashed line separates region A ($P_r \leq 1$) from region B ($P_r > 1$).

promptly at recollision, the relevant vector potential would be $A(t_r)$. Because recollision occurs close to a zero of the electric field, $|A(t_r)|$ is generally large and sizable drift momenta are expected. A localized low-P_r anticorrelation therefore points to a post-recollision near-core configuration that survives until a later field window, where double escape is completed with small longitudinal drift. This interpretation is consistent with the RIET picture used in semiclassical models below the recollision threshold.[12] In that picture, recollision does not necessarily remove the second electron immediately; instead, it prepares an excited or strongly correlated configuration that can persist into a later field window. It is also in line with recent attoclock measurements of correlated-electron emission and with theoretical studies showing that recollision-induced-excitation pathways leave final two-electron momentum distributions that depend on field symmetry and quantum interference.[22,35–38] In the present trajectories, the low-P_r component is associated with a post-recollision near-core configuration whose final escape occurs in a later field window close to an electric-field maximum, where the vector-potential contribution to the longitudinal drift is small.

The role of the final field phase in producing the low-P_r component is examined in Fig. 3. The figure compares three trajectory ensembles: from the full NSDI ensemble to the anticorrelated sector (region A + B) and then to its small radial momentum component (region A). The four columns resolve the initial tunneling phase, the recollision phase, the phase at which double ionization is completed, and the delay $\Delta t = t_{ion} - t_r$. The tunneling phase characterizes the launch of the first electron, the recollision phase characterizes the return and energy-transfer step, and the final double-ionization phase characterizes when the asymptotic drift momentum is imprinted. The red field reference curves in Fig. 3 distinguish electric-field maxima from field zero crossings. This distinction is important because prompt recollision occurs near field zero crossings, where $|A(t_r)|$ is large, whereas small final longitudinal drift is favored when double escape is completed near field maxima, where the vector potential is small.

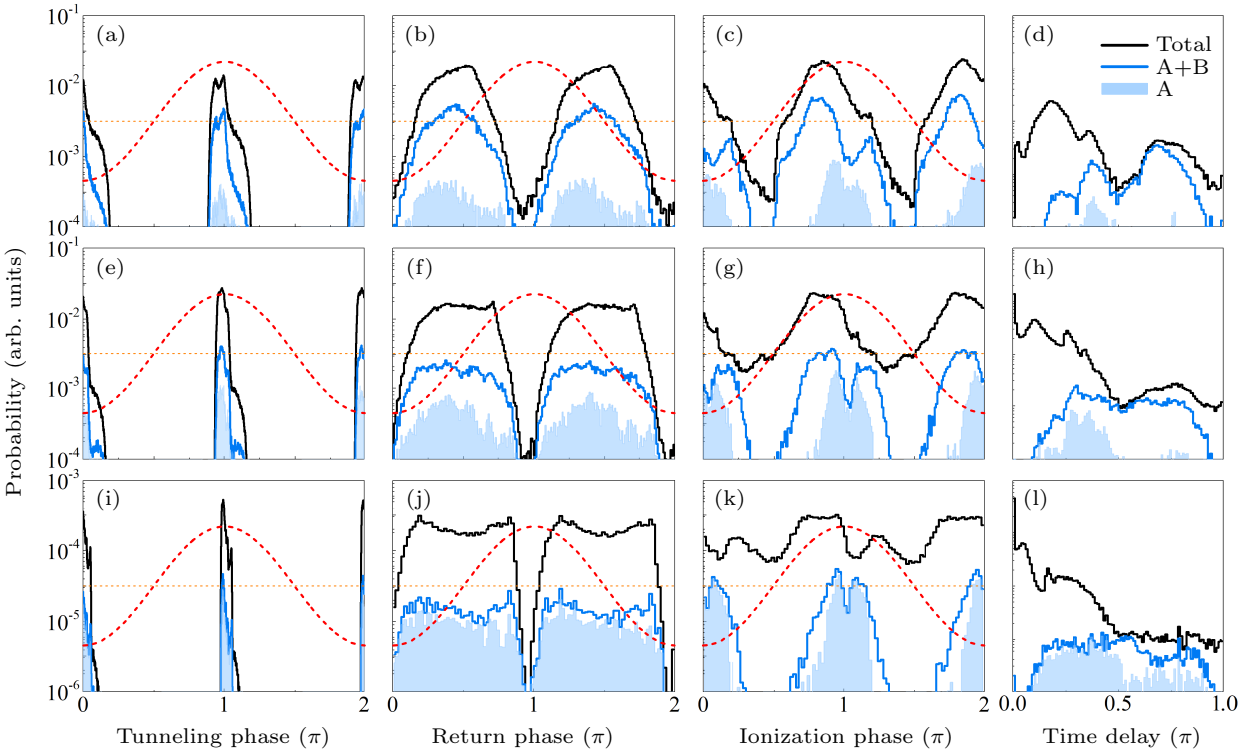


Fig. 3. Phase and delay diagnostics for double-ionization trajectories at 800 nm (top row), 1300 nm (middle row), and 3100 nm (bottom row). Columns show the initial tunneling phase, recollision phase, final double-ionization phase, and delay $\Delta t = t_{ion} - t_r$. Black, blue, and light-blue distributions correspond to all double-ionization events, anticorrelated-sector events A+B, and the low-momentum subset A, respectively. Red guides mark the laser field and its zero level, showing that low-P_r events are finally emitted near field maxima.

The first two columns show that the tunneling and return phases of the anticorrelated region A + B largely follow those of the full double-ionization ensemble. The initial ionization is gated near the field maxima, as expected from the ADK rate, while the recollision occurs in the usual return window close to the field zero crossings. At 3100 nm, additional later-return contributions are visible, consistent with the longer electron excursion in the mid-infrared field. Since recollision occurs close to field zero crossings, double ionization completed promptly at recollision would generally lead to considerable longitudinal drift.

The third column in Fig. 3 gives the phase at which double ionization is completed. In contrast to the broader anticorrelated region A + B at shorter wavelengths, the low-P_r sub-

set A is concentrated near the maxima of the electric field. With increasing wavelength, the longer excursion time and stronger wave-packet spreading reduce the relative weight of close near-core returns that lead to large-angle backscattering in the anticorrelated sector. As a result, the high-P_r backscattering tail becomes less prominent, while delayed field ionization near the field maxima gives a larger contribution to A+B, making its final-ionization phase distribution approach that of subset A. Therefore, the vector-potential contribution to the final longitudinal momenta is small, leading to small $p_{1,z}$, $p_{2,z}$.

The fourth column in Fig. 3 demonstrates the delay between the closest recollision and the completion of double ionization, which provides the time-ordering information of the ionization process. Small Δt corresponds to prompt release after recollision, whereas finite Δt indicates post-recollision emission. With increasing wavelength, the delay distribution of the low-P_r subset A shifts toward larger Δt, indicating that anticorrelated emission is increasingly later after recollision. The results reflect the reduced role of prompt large-angle backscattering in the low-P_r sector and the enhanced importance of recollision-induced excitation followed by field ionization in a later field. Together with the third-column phase distribution in Fig. 3, the finite-delay behavior shows that the low-P_r signal is associated with delayed escape near field maxima, rather than with prompt release at the recollision time.

3.3. Angular signatures of low- and high-momentum anticorrelation

Figure 4 compares the normalized polar emission-angle distributions for regions A and B. The angle is measured with respect to the laser polarization axis. Region B corresponds to larger final longitudinal drift momenta and therefore shows stronger alignment with the polarization axis. In contrast, in region A the longitudinal drift momentum is suppressed, so the final emission angle becomes more sensitive to transverse momentum and to the post-recollision Coulomb interactions, resulting in a broader oblique angular distribution.

The wavelength dependence of region A reflects the changing competition between prompt recollision-impact ionization and delayed field ionization following recollision-induced excitation. At 800 nm and 1300 nm, the low-P_r subset still retains oblique lobes, indicating that transverse momentum and Coulomb momentum exchange after recollision remain important. At longer wavelengths, wave-packet spreading during the extended excursion before recollision reduces the near-core return flux and thus weakens prompt recollision-impact ionization, which requires a close recollision and efficient energy transfer. The low-P_r sector is therefore preferentially populated by recollision-induced excitation followed by delayed field ionization. At 3100 nm, this delayed field-ionization step occurs preferentially near electric-field maxima, where $A(t_{ion}) \simeq 0$. This keeps P_r low, while the field-lowered barrier favors release along the laser polarization direction, leading to enhanced yield near $\theta \approx 0°$ and 180°. Thus, the broad and structured angular distribution of region A results from the combined effect of the final escape phase, transverse momentum, and post-recollision Coulomb dynamics.

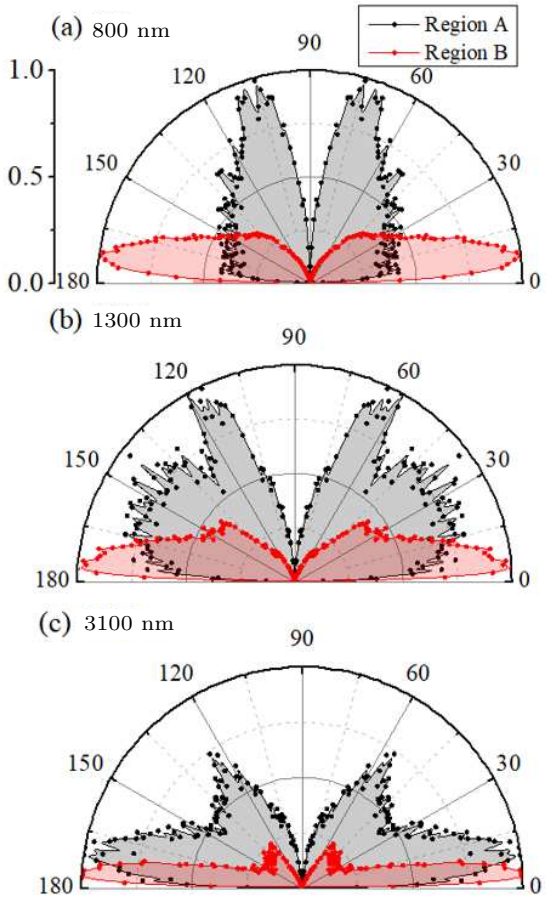


Fig. 4. Normalized polar emission-angle distributions for low- and high-momentum anticorrelated trajectories. Panels correspond to (a) 800 nm, (b) 1300 nm, and (c) 3100 nm. Black curves denote region A ($P_r \leq 1$), and red curves denote region B ($P_r > 1$).

4. Conclusion

We have studied wavelength-dependent nonsequential double ionization of Ar with a full-Coulomb three-dimensional semiclassical model including quasistatic tunneling, microcanonical sampling of the second electron, electron–core and electron–electron Coulomb propagation, and field ionization from transient excited configurations. The calculated momentum spectra show that the mid-infrared regime is not obtained by a simple $\sqrt{U_p}$ rescaling of the near-infrared spectrum. The high-momentum fingerlike structures at 800 nm and 1300 nm are associated with the backscattering branch of the recollision dynamics, where the returning electron undergoes a close near-core encounter and a Coulomb-assisted reversal of its longitudinal velocity. At 3100 nm, longer excursions and stronger wave-packet spreading reduce the relative weight of this close backscattering

branch, while forward-scattering-like recollision trajectories and the crosslike central structure become more prominent. The low-momentum anticorrelated emission in quadrants II and IV has a different dynamical origin. It is traced to a post-recollision near-core configuration that survives until a later field-ionization window. Phase- and delay-resolved diagnostics show that double escape is completed near maxima of the electric field, where the vector-potential contribution to the longitudinal drift is small. Thus, the low-P_r component is not determined by recollision energy alone; it also records the field phase at final escape. These results provide a trajectory-level interpretation of low-momentum anticorrelated electron emission in mid-infrared double ionization. They show that high-U_p correlated spectra should be read through two coupled ingredients: recollision kinematics, which shapes the global momentum distribution, and post-recollision field ionization, which produces the low-momentum anticorrelated component. Extensions beyond the dipole approximation and fully quantum interference effects remain important for long-wavelength double ionization.

Acknowledgments

Shiwei Liu acknowledges helpful discussion with Mr. Zhihe Zhang from Peking University. Project supported by the National Natural Science Foundation of China (Grant Nos. 12588301, 12574370, and 12404329) and the Cultivation Project Funds for BUCEA (Grant No. X24006).

References

[1] Corkum P B 1993 *Phys. Rev. Lett.* **71** 1994
[2] Fittinghoff D N, Bolton P R, Chang B and Kulander K C 1992 *Phys. Rev. Lett.* **69** 2642
[3] Walker B, Sheehy B, DiMauro L F, Agostini P, Schafer K J and Kulander K C 1994 *Phys. Rev. Lett.* **73** 1227
[4] Weber Th, Giessen H, Weckenbrock M, Urbasch G, Staudte A, Spielberger L, Jagutzki O, Mergel V, Vollmer M and Dörner R 2000 *Nature* **405** 658
[5] Moshammer R, *et al.* 2002 *Phys. Rev. A* **65** 035401
[6] Weckenbrock M, *et al.* 2003 *Phys. Rev. Lett.* **91** 123004
[7] Staudte A, *et al.* 2007 *Phys. Rev. Lett.* **99** 263002
[8] Rudenko A, de Jesus V L B, Ergler Th, Zrost K, Feuerstein B, Schröter C D, Moshammer R and Ullrich J 2007 *Phys. Rev. Lett.* **99** 263003
[9] Becker W, Liu X, Ho P J and Eberly J H 2012 *Rev. Mod. Phys.* **84** 1011
[10] Feuerstein B, *et al.* 2001 *Phys. Rev. Lett.* **87** 043003
[11] Shaaran T, Nygren M T and Figueira de Morisson Faria C 2010 *Phys. Rev. A* **81** 063413
[12] Ye D F and Liu J 2010 *Phys. Rev. A* **81** 043402
[13] Wang P Z, Qian L J, Sun Z R and Yang Y 2024 *Chin. Phys. B* **33** 063201
[14] Chen J H, Xu T T, Han T, Sun Y, Xu Q Y and Liu X S 2020 *Chin. Phys. B* **29** 013203
[15] Chen Z, Morishita T, Le A T, Wickenhauser M, Tong X M and Lin C D 2010 *Phys. Rev. Lett.* **104** 253201
[16] Ye D F, Liu X and Liu J 2008 *Phys. Rev. Lett.* **101** 233003
[17] Liu Y Q, Ye D F, Liu J, Rudenko A, Tschuch S, Dürr M, Siegel M, Morgner U, Gong Q H, Moshammer R and Ullrich J 2010 *Phys. Rev. Lett.* **104** 173002
[18] Fu L B, Xin G G, Ye D F and Liu J 2012 *Phys. Rev. Lett.* **108** 103601
[19] Hao X L, Chen J, Li W D, Wang B B, Wang X D and Becker W 2014 *Phys. Rev. Lett.* **112** 073002
[20] Maxwell A S and Figueira de Morisson Faria C 2016 *Phys. Rev. Lett.* **116** 143001
[21] Quan W, *et al.* 2017 *Phys. Rev. A* **96** 032511
[22] Liu S W, Ye D F, Jiang Y H and Liu J 2023 *Commun. Phys.* **6** 282
[23] Wang Z Q, *et al.* 2025 *Chin. Phys. Lett.* **42** 053701
[24] Ye D F, Li M, Fu L B, Liu J, Gong Q H, Liu Y Q and Ullrich J 2015 *Phys. Rev. Lett.* **115** 123001
[25] Wolter B, *et al.* 2015 *Phys. Rev. X* **5** 021034
[26] Li Y B, Wang X, Yu B H, Tang Q B, Wang G H and Wan J G 2016 *Sci. Rep.* **6** 37413
[27] Sun X, Li M, Ye D F, Xin G G, Fu L B, Xie X G, Deng Y K, Wu C Y, Liu J, Gong Q H and Liu Y Q 2014 *Phys. Rev. Lett.* **113** 103001
[28] Yuan Z Q, Liu J, Fu L B and Ye D F 2016 *Phys. Rev. A* **93** 063409
[29] Wang Y L, Xu S P, Quan W, Gong C, Lai X Y, Hu S L, Liu M Q, Chen J and Liu X J 2016 *Phys. Rev. A* **94** 053412
[30] Wang Y L, *et al.* 2017 *Phys. Rev. A* **95** 063415
[31] Jia X, Guo L, Hao X, Becker W and Chen J 2024 *Phys. Rev. A* **109** 023105
[32] Thiede J H and Prauzner-Bechcicki J S 2024 *Phys. Rev. A* **110** 053105
[33] Li Y B, *et al.* 2025 *Chin. Phys. Lett.* **42** 053703
[34] Shaaran T, *et al.* 2019 *Phys. Rev. A* **99** 023421
[35] Wang Y L, Yu S G, Sun R P, Kang H P, Xu S P, Lai X Y, Quan W and Liu X J 2024 *Phys. Rev. Lett.* **132** 223202
[36] Hashim S, Tenney R and Figueira de Morisson Faria C 2024 *Phys. Rev. A* **109** 063110
[37] Hashim S, Habibović D and Figueira de Morisson Faria C 2025 *Phys. Rev. A* **112** 023118
[38] Hashim S, Habibović D and Figueira de Morisson Faria C 2025 *Phys. Rev. A* **112** 023119
[39] Liu J 2013 *Classical Trajectory Perspective of Atomic Ionization in Strong Laser Fields: Semiclassical Modeling* (New York: Springer)
[40] Ammosov M V, Delone N B and Krainov V P 1986 *Sov. Phys. JETP* **64** 1191
[41] Leopold J G and Percival I C 1979 *J. Phys. B* **12** 709
[42] Reinhold C O and Falcón C A 1986 *Phys. Rev. A* **33** 3859
[43] Volkov D M 1935 *Z. Phys.* **94** 250
[44] Lewenstein M, Balcou P, Ivanov M Yu, L'Huillier A and Corkum P B 1994 *Phys. Rev. A* **49** 2117
[45] Kübel M, *et al.* 2013 *Phys. Rev. A* **88** 023418
[46] Huang C, Zhou Y, Zhang Q and Lu P 2013 *Opt. Express* **21** 11382
[47] Xin G G, Ye D F and Liu J 2010 *Phys. Rev. A* **82** 063423
[48] Fan G Q, Yang Z J, Sun F H, Zheng J M, Han Y T, Huang M Q and Liu Q C 2024 *Chin. Phys. B* **33** 083102